PCCP

PAPER

View Article Online
View Journal | View Issue

Cite this: *Phys. Chem. Chem. Phys.*, 2016, **18**, 26796

Ice nucleation on nanotextured surfaces: the influence of surface fraction, pillar height and wetting states†

Atanu K. Metya,[a] Jayant K. Singh*[a] and Florian Müller-Plathe[b]

Received 22nd June 2016,
Accepted 24th August 2016

DOI: 10.1039/c6cp04382h

www.rsc.org/pccp

In this work, we address the nucleation behavior of a supercooled monatomic cylindrical water droplet on nanoscale textured surfaces using molecular dynamics simulations. The ice nucleation rate at 203 K on graphite based textured surfaces with nanoscale roughness is evaluated using the mean fast-passage time method. The simulation results show that the nucleation rate depends on the surface fraction as well as the wetting states. The nucleation rate enhances with increasing surface fraction for water in the Cassie–Baxter state, while contrary behavior is observed for the case of Wenzel state. Based on the spatial histogram distribution of ice formation, we observed two pathways for ice nucleation. Heterogeneous nucleation is observed at a high surface fraction. However, the probability of homogeneous ice nucleation events increases with decreasing surface fraction. We further investigate the role of the nanopillar height in ice nucleation. The nucleation rate is enhanced with increasing nanopillar height. This is attributed to the enhanced contact area with increasing nanopillar height and the shift in nucleation events towards the three-phase contact line associated with the nanotextured surface. The ice-surface work of adhesion for the Wenzel state is found to be 1–2 times higher than that in the Cassie–Baxter state. Furthermore, the work of adhesion of ice in the Wenzel state is found to be linearly dependent on the contour length of the droplet, which is in line with that reported for liquid droplets.

1 Introduction

The formation and growth of ice from supercooled water are ubiquitous[1,2] and play an important role in different processes, ranging from the Earth's atmosphere[3,4] to nanoscale processes.[5] However, many fundamental aspects of ice nucleation are still not well understood, though a large number of experimental and theoretical studies have been conducted on the nucleation phenomena.[6–8] The ice nucleation events start from either two or three interfaces such as liquid–solid, vapor–liquid and vapor–liquid–solid.[8] A good ice promoting surface has the ability to form an ice-like ordered structure through surface–fluid interactions and surface templating effects[9–11] with water molecules. On the other hand, surface roughness plays a vital role in the anti-icing performance of surfaces through freezing delay or eliminating ice formation.[12–14] Thus, superhydrophobic surfaces have been considered as one of the promising ice-repellent materials.[12,13,15]

Hydrophobicity of a surface is generally characterised by measuring the contact angle of a water droplet. The behavior of a liquid droplet on a rough surface is typically governed by the wetting states *viz.*, the Cassie–Baxter state[16] and the Wenzel state.[17] The Cassie–Baxter state is defined as a state where a liquid droplet is suspended on the top of a rough surface and air is trapped in the hollow spaces of the rough surface (Fig. 1, left). On the other hand, in the Wenzel state, a liquid droplet completely fills the space between the surface grooves and wets the solid substrate (Fig. 1, right). Several studies have reported the effect of surface roughness at the micro- and nano-scales on ice nucleation and found that superhydrophobic surfaces have an excellent ice repellent character with low ice adhesion strength.[14,15,18] However, there are studies on superhydrophobic surfaces which have reported both significant freezing delay[13,18] as well as promotion of ice nucleation.[15,19] For example, Alizadeh *et al.*[18] have found that high contact angles on superhydrophobic surfaces lead to a lower interfacial area between the water and the surface, resulting in an enhanced free energy barrier for nucleation causing freezing delay. In contrast, Jung *et al.*[15] have found

[a] *Department of Chemical Engineering, Indian Institute of Technology Kanpur, Kanpur-208016, India. E-mail: jayantks@iitk.ac.in; Fax: +91-0512-259-0104; Tel: +91-0512-259-6141*

[b] *Eduard-Zintl-Institut für Anorganische und Physikalische Chemie and Center of Smart Interfaces, Technische Universität Darmstadt, Petersenstrasse 22, D-64287 Darmstadt, Germany*

† Electronic supplementary information (ESI) available: Details of the bond-orientational order parameters, the CHILL algorithm, the MFPT method, the phantom-wall algorithm, and additional results of this work. See DOI: 10.1039/c6cp04382h

Fig. 1 A schematic illustration of the Cassie–Baxter state (left) and the Wenzel state (right).

significant longer freezing delays on hydrophilic surfaces (higher wettability) with nanometer-scale roughness compared to superhydrophobic surfaces (lower wettability) with larger roughness values. Under subzero conditions, due to the condensation of water vapor on a superhydrophobic surface the resulting drops prefer the Wenzel state leading to higher adhesion strengths.[20] Thus, superhydrophobic surfaces in such cases are not suitable for anti-icing applications. Hence, many investigations have been carried out on the development of low surface energy materials such as polymers, fluorocarbons and silicone precursors[21,22] for improving the anti-icing capability of nanostructured materials. Nevertheless, to design a suitable material for improving anti-icing efficiency in various industrial processes and applications such as power transmission lines, aircraft wings, wind turbines, ships and buildings, efforts are required to understand the principle underlying the mechanism of ice nucleation. Thus, it is imperative to understand the effect of nanostructure surfaces on the nucleation behavior of supercooled water.

Several groups have studied the effect of surface energy and roughness of the textured surfaces on the nucleation and adhesion behavior of supercooled water.[12,15,20,22–24] Mueler *et al.*[12] found a linear relationship between ice-adhesion strength and practical work of adhesion. Recent work by Singh and Müller-Plathe[20] found that the ice adhesion on the superhydrophilic surfaces dramatically increases for ice droplets in the Wenzel state, which would be the case if there is a phase transition from the Cassie–Baxter state to the Wenzel state under supercooled conditions. Recently, Fu *et al.*[22] studied the ice nucleation behavior on sol–gel coatings with a wide range of surface energies and roughness. They found that upon increasing the amount of fluoroalkylsilane (FAS) additive, the water droplets transform from the Wenzel state into the Cassie–Baxter state with a two orders of magnitude higher nucleation rate. Based on the results, the authors concluded that heterogeneous nucleation starts at the solid–liquid interface as well as at the three-phase contact line. Jung *et al.*[25] experimentally captured the location of nucleation at the water–air interface of supercooled droplets on super-hydrophobic surfaces in the presence of a gas stream. The results suggested that the surface roughness and environmental conditions can alter the ice nucleation and nuclei growth mechanisms.

In experiments, the accurate capture of nucleation events as well as quantification of the freezing process is difficult due to practical challenges in designing relevant experiments. However, in this direction, computational simulations[26,27] play an important role in the study of nucleation processes. The homogeneous nucleation of ice has been extensively studied by several research groups using molecular dynamics (MD) and Monte Carlo (MC) simulations.[11,28–36] On the other hand, relatively few works have been reported on the ice nucleation behavior of supercooled water droplets on smooth and rough surfaces.[7,10,20,37–39] A recent study of Zhang *et al.*[37] showed that surface morphology has a remarkable effect on ice nucleation. The authors suggest that the enhancement in the nucleation rate on nanostructured surfaces is mainly due to the commensurability of the characteristic length of ice with the groove width. However, an understanding of the effect of surface fraction, pillar height and wetting states on the ice nucleation is far from complete, which we have investigated in this study. Thus, in this work our motivation is to provide molecular insights into the ice nucleation mechanism on nanostructured surfaces using molecular dynamics simulations.

2 Model and simulation details

A schematic of the building block (unit cell) of a textured surface is shown in Fig. 2A (top and side views). The textured surfaces are designed using two atomic layers of graphene (AB stacking) as the base layer. An artificial pillar made out of additional graphite sheets is used on top of the base layer. The width and the gap between two pillars are varied in the range of 0.5–2.0 nm in both x and y directions. The atomic structure of the top the pillar layer of the graphite sheet is represented in Fig. 2B (for a few systems). In this work, we have considered pillar heights of 4, 6, 8, 10, and 12 atomic layers of graphene sheets, corresponding to h = 1.36, 2.04, 2.72, 3.4 and 4.08 nm, respectively. We define surface fraction, α, as the ratio of the projected area of the pillar to the area of the base cross-section. In this work, α is varied from 0.089 to 0.536. The lateral dimension of the simulation system is fixed to 3.4 nm $\times$ 15.5 nm. A typical water droplet used in this work contains 2000 water molecules in a cylindrical shape with a length of 3.4 nm. A representative snapshot of a water droplet placed on a textured surface is shown in Fig. 2C. In order to create Wenzel states for a cylindrical water droplet at lower α values ($\alpha \leq 0.223$), first, we have applied instantly a downward velocity to all the water molecules. The downward velocity is retained until molecules reach the bottom of the grooves. Subsequently, the downward

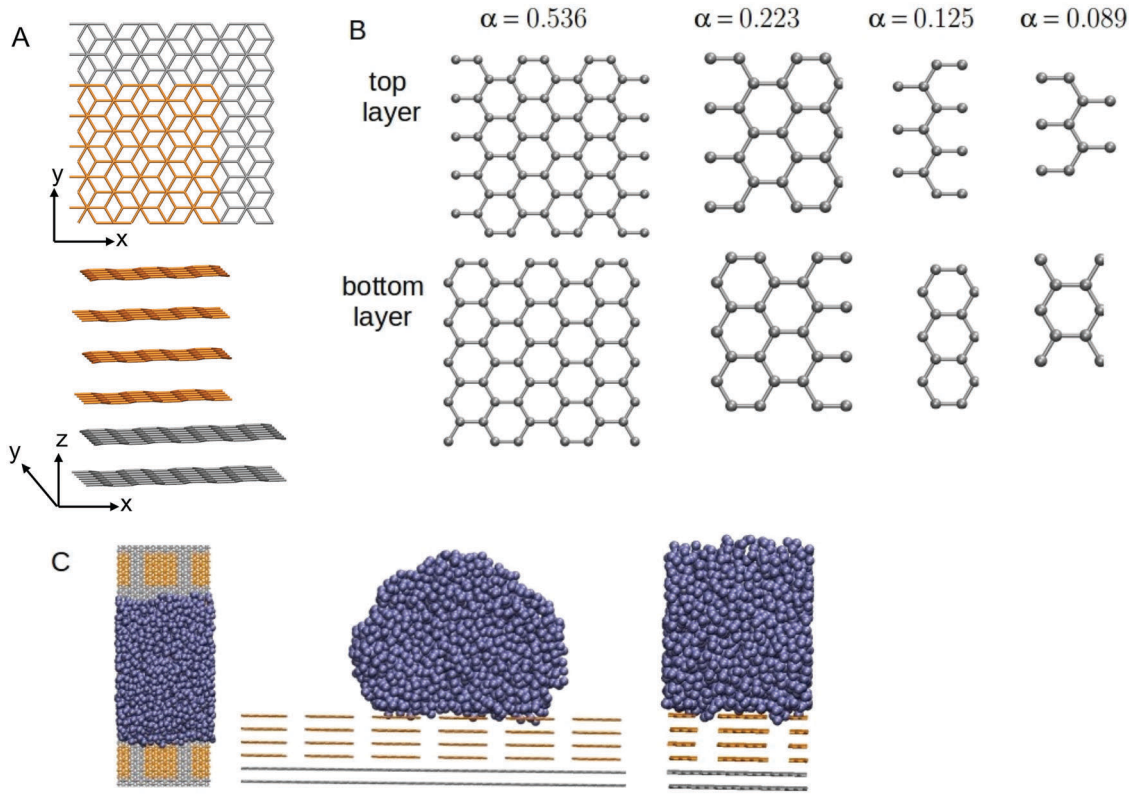

Fig. 2 (A) A schematic representation of side and top views of the unit cell of a textured surface used in the current work. Pillar and base layers are represented by orange and gray color lines. (B) Representative atomic structures of the top (first row) and bottom (second row) layers of a graphite sheet of textured surfaces with different surface fraction (α) values. (C) Top and side views of a simulation system used for the study. The water molecules are represented as solid balls (ice blue color).

velocity is removed and the linear momentum of the water is zeroed. A similar approach is adopted by Koishi *et al.*[40]

A coarse-grained monatomic model of water, the mW[41] model, is used. The potential function of the mW model includes two terms, a two-body term and a three-body term. The interaction between the water molecules and the surface atoms is modeled by the two-body term of the mW model. In this work, all the cross-interaction parameters are adopted from a recent parameterization of the mW model by Lupi *et al.*,[7] which reproduces the experimental contact angle of water on a smooth graphite surface.

All simulations are performed using the LAMMPS simulation package[42] in a canonical ensemble. The velocity-Verlet algorithm is used for integrating the equations of motion of water molecules with a time step of 10 fs in all the systems. The temperature is controlled by a Nosé–Hoover thermostat with a relaxation time of 1.0 ps. Periodic boundary conditions are applied in the x and y directions, while the z direction is non-periodic and bounded with a reflective wall. The surface atoms are kept fixed during the simulations. The cylindrical water droplet on the textured surface is initially equilibrated for 40 ns at a temperature of 300 K. An additional 100 ns simulations are performed to collect a large number of independent trajectories (different configurations are selected at 1.0 ns intervals) from the equilibrated system. Subsequently, using individual independent trajectories as a starting configuration, the temperature of the system is instantaneously quenched from 300 to 203 K, and the system is allowed to crystallize within a timescale of 300 ns. The trajectories are collected after every 1000 steps for estimating the nucleation rate.

In simulations of supercooled water, the bond orientational parameters q_3 and q_6 are often used to identify the ice-like molecule from supercooled water and has been used effectively in nucleation studies.[10,32,33,39,43] Among q_3 and q_6 order parameters, q_6 is insufficient to differentiate cubic and hexagonal ice.[32] In the present study, we thus used q_3 as a bond orientational order parameter to identify ice-like molecules from supercooled water. We have used the CHILL algorithm[43] to identify crystalline clusters in the nucleation study. A detailed description of the algorithm along with other details is provided in the ESI.† In order to evaluate the nucleation rate of supercooled water, we adopt the mean first-passage time (MFPT) method[44] in our study (see the ESI†). The method has been used by various authors,[31,37] due to its inherent ability to directly provide the nucleation time, the size of the critical nuclei, and the location of the nucleation barrier by fitting the MFPT curve using the following expression:[44]

$$\tau(n) = \frac{\tau_J}{2}\{1 + \mathrm{erf}[(n - n^*)c]\}, \quad (1)$$

where $\tau(n)$ is the MFPT as a function of n, obtained by averaging over several nucleation simulations with different initial configurations.

τ_J and n^* are the nucleation time and the critical nuclei size, respectively. The parameter c is a constant which is related to the Zeldovich factor, Z, as $c = Z\sqrt{\pi}$. The nucleation rate J is estimated from the volume V of the water droplet and the time of nucleation τ_J, $J = 1/(\tau_J V)$. The volume is calculated from the molecular volume of ice in the mW model.[11] In the present study, we have used more than 50 independent successful nucleation simulations for the calculation of nucleation rate.

3 Results and discussion

First, we have evaluated the freezing temperature of a cylindrical water droplet. The freezing temperature of ice is determined by obtaining the temperature at which a sharp change in the potential energy is observed along with a jump in the largest ice-like cluster. To this end, we have performed 6–8 independent cooling temperature ramp simulations with a constant cooling rate. The freezing temperature for the cylindrical water droplet containing 2000 water molecules, with a cooling rate of 1 K ns^{-1}, is 192 ± 3 K. Thus, the relative undercooling with respect to the bulk melting temperature[45] for a cylindrical droplet ($\Delta T = T_m^{bulk} - T$) is 82 K. The freezing temperature obtained in this work is in line with that of a spherical water nanodroplet with 2149 water molecules, with a cooling rate of 0.5 K ns^{-1}.[11] However, the freezing temperature for the same size of the water droplet is lower than the melting temperature, $T_m = 237 \pm 2$ K. We have also determined the freezing temperature of the bulk water with cooling rates of 1 and 0.1 K ns^{-1}, which are 198 ± 3 K and 202 ±2 K, respectively. Moreover, the rate of nucleation of bulk water is estimated to be $4.1 \pm 0.12 \times 10^{33}$ m^{-3} s^{-1} at 203 K using the MFT method. These values are in good agreement with the prediction of Moore and Molinero.[31] Ice cystallization of the bulk mW water, at a temperature below 202 K, undergoes simultaneous nucleation and growth, as shown by Moore and Molinero,[31] which is reflected in the MFPT plot having no clear plateau. In order to avoid fast crystallization for a cylindrical droplet on the nanostructured surfaces, we have considered the nucleation temperature at 203 K, which is more than 10 K above the freezing temperature at which the crystallization mechanism of mW water transforms from nucleation-dominated into growth-dominated. At this temperature, we found a sufficient number of nucleation phenomena within the time-scale accessible in our simulation time. On the other hand, no crystallization was observed within 400 ns for the water droplet at a temperature of 203 K, based on 50 independent simulations.

Next, we have estimated and compared the rate of crystallization of water droplets on different nanotextured surfaces. The nucleation rate at 203 K on various nanotextured surfaces considered in the present work as a function of α is shown in Fig. 3, where the water droplets are in Cassie–Baxter and Wenzel states. In the case of the Cassie–Baxter state, the rate of nucleation slightly enhances with increasing α. On the other hand, for the Wenzel state, the nucleation rate apparently increases with decreasing α. The estimated nucleation rate in this work indicates that nanostructured surfaces inhibit ice nucleation. This is in line with the results of Cox *et al.*[10]

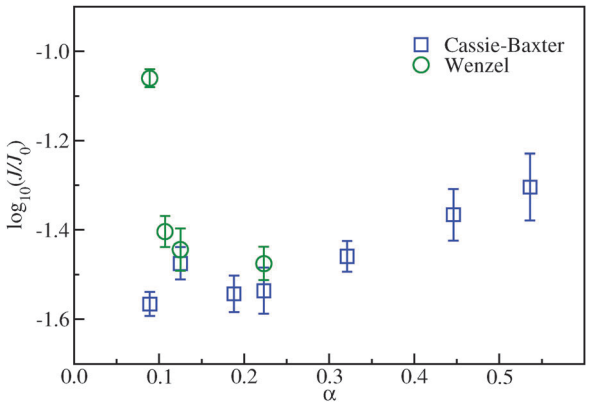

Fig. 3 The ice nucleation rate as a function of surface fraction at 203 K, for different nanostructured surfaces with pillar height, h = 0.136 nm. The values of the ice nucleation rate are expressed as $\log_{10}(J/J_0)$, where J_0 refers to the nucleation rate of bulk water at the same temperature. The error bars are the standard deviation of the block averages.

where the ice nucleation rate of a hydrophilic nanoparticle was found lower than the bulk water at 205 K. Recently, Fitzner *et al.*[39] calculated ice nucleation of a water film on various planes of the fcc crystal with varying lattice constants and surface–fluid interactions. The authors found that lattice mismatch can inhibit ice nucleation. The size of the critical nucleus varies slightly for different nanotextured surfaces considered in this work, with a value of 42 ± 3. This value is in line with the previously reported critical nuclei size in the literature, *e.g.* 10 ± 2 and 50 at 205 K for crystallization of water on rough[37] and smooth[39] surfaces, respectively. First, we will describe the nucleation behavior of a water droplet in the Cassie–Baxter state. The enhancement of the nucleation rate is observed at higher α values, whereas the rate remains roughly constant for the lower range of α ($\alpha < 0.223$). However, the obtained nucleation rate is approximately 35 times slower than the bulk homogeneous nucleation for the lower range of α. Interestingly, higher nucleation rate is observed at α = 0.125 (higher structural roughness) compared to α = 0.223 (lower structural roughness). This result implies that the presence of the structural roughness of the top of the pillar promotes the ice nucleation. To verify this conjecture, we compute the crystallization temperature of water droplets on the rough surfaces at lower values of α. We have performed 4–6 independent simulations with a cooling rate of 0.5 K ns^{-1}, each starting at a temperature of 230 K, which is above the freezing temperature. The crystallization temperatures obtained for α = 0.223, 0.125, and 0.089 are 198 ± 1 K, 195 ± 2 K and 195 ± 3 K, respectively. Interestingly, the crystallization temperature does not reflect any effect of the surface fraction clearly. It is surprising though that with decreasing α, the area of contact between the water and the nanostructured surface also decreases. Thus, we expect less effect of the surface, which is more clearly seen in the nucleation rate for α = 0.089 (as will be discussed in a later section of the article).

The freezing process of a supercooled water droplet on the surface proceeds in three sequential stages. In the first stage,

ice-like water molecules form a critical nucleus. This is followed by a very rapid phase transition and then it enters into the slow growth process, in which the remaining liquid freezes isothermally. From a thermodynamic perspective,[8] there are three spatial preferences for the formation of the critical nuclei, *i.e.* near the vapor–liquid, liquid–substrate or vapor–liquid–substrate region. The homogeneous nucleation of the slab of water with two free surfaces has been studied through atomistic simulations, and it was found that freezing preferentially occurs at the subsurface (*i.e.* a water layer away from the vapor–liquid interface), though

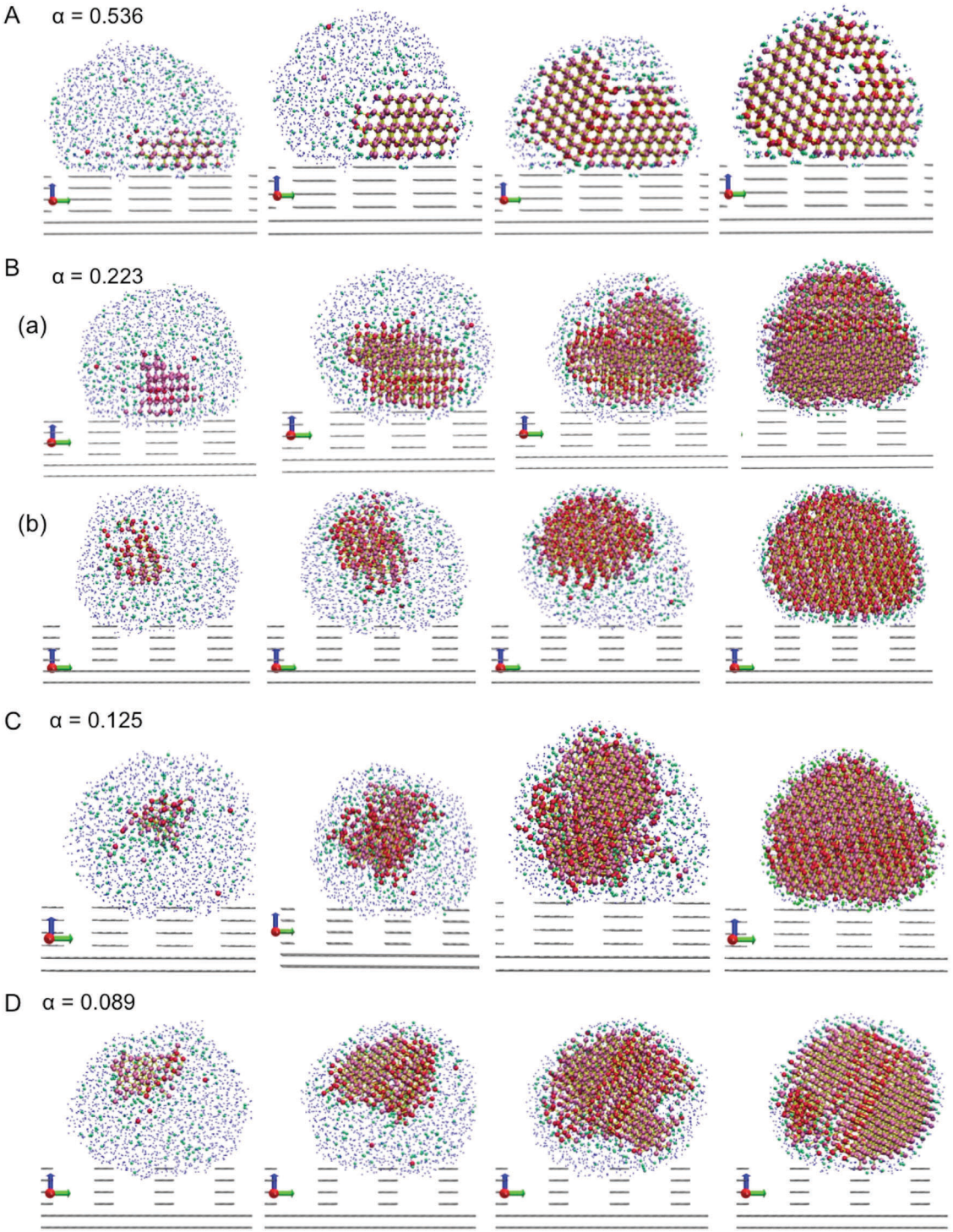

Fig. 4 Snapshots of crystallization trajectory of supercooled water on different nanotextured surfaces. (A) α = 0.536 and (B) α = 0.223; a and b represent the nucleation in heterogeneous and homogeneous manners, respectively, (C) α = 0.125, and (D) α = 0.089. The colors light red, red, green and blue represent water molecules in cubic ice, hexagonal ice, intermediate ice (ESI†) and liquid water, respectively.

it was also observed in the bulk region of the slab.[46] On the other hand, in a recent work on the crystallization of a mW water nanodroplet using MD simulations,[11] it was reported that the nucleation starts randomly within the nanodroplets. The authors did not observe any preferential location at the interface of the supercooled water nanodroplets. In a heterogeneous nucleation process, the substrate mostly promotes the crystallization. According to our simulation results, at α greater than 0.223, most of the heterogeneous nucleation events start near the top of the pillar surface as shown in Fig. 4A. At α = 0.223, the nucleation events start either in the vicinity of the top of the pillar surface (see Fig. 4B(a)) in a heterogeneous manner or away from the surface in a homogeneous fashion (see Fig. 4B(b)). At α less than 0.223, the ice nucleation events occur away from the top of the surface and the vapor–liquid interface *i.e.* in the homogeneous manner as shown in Fig. 4C and D. Recently, Cox *et al.*[10] also observed the homogeneous manner of nucleation of water in the presence of a structured (hexagonal) nanoparticle (NP) at weak water–NP interaction. Homogeneous-like nucleation is observed at lower α values due to the decrease in the interfacial area between the surface atoms and the water molecules, which reduces the effective interaction. Thus, lower α does not promote the formation of ice-like structures of water molecules near the surface, which otherwise promotes the heterogeneous nucleation. This is in line with the reduction of nucleation rates for lower values of α as seen in Fig. 3.

In order to understand the favorable locations of the cluster formation at different stages of crystallization and the structural behavior of water molecules above the various textured surfaces, we now examine the spatial cluster distribution of the ice nucleus and the water density profile along the *z*-direction normal to the surface. Here, we have considered two spatial regions: near the substrate and away from the surface, which are defined as the region with height less than 1.0 nm and greater than 1.0 nm from the top of the substrate, respectively. In order to identify the location of cluster formation at different stages of nucleation, we have chosen arbitrarily three different cluster sizes: 40–45, 70–75, and 140–150. The first time appearance of a cluster of a chosen size range is recorded in a histogram distribution. The distribution is based on the lower boundary of an ice cluster (minimum value of the *z*-coordinate) along the *z*-axis. The fraction of the spatial location of the cluster formation is plotted as a function of distance from the surface. Fig. 5 illustrates the different sizes of the largest cluster distributions at different stages of cluster formation. The propensity to form smaller size ice clusters (40–45) near the surface (0–1.0 nm) reduces with α; whereas the histogram distribution values of ice nuclei above 1.0 nm from the surface increases with decreasing α as shown in Fig. 5a. From Fig. 5b and c, it is clear that as the ice clusters grow, the tendency to grow from an ice nucleus is favorable near the surface (0–1.0 nm). Furthermore, we have analysed the distribution of ice clusters at different stages of nuclei formation along the direction normal to the surface (see the ESI,† Fig. S3). The figures illustrate that at higher α values (α = 0.536) the tendency to form ice nuclei is higher on the top of the surfaces as compared to the lower α values, while the formation of large ice clusters is also favored away from the solid–liquid interface.

Fig. 6 presents the snapshots of representative nucleation events as well as density profiles of water molecules along the direction normal to the surface. At α = 0.536, the in-plane structure of the contact layer ice-like molecules forms a hexagonal symmetry which is compatible with the basal face of ice, as depicted in Fig. 6A (top view). We also found that ice-like water molecules form a hexagonal arrangement on the top of the nanostructured surface followed by rapid growth towards the vapor–liquid interface (see the ESI,† Fig. S4). The density profile of water molecules along the direction normal to the surface clearly shows that a water layer is formed on the top of the nanostructured surface. Furthermore, Fig. 6A (side view) shows that the prism face of ice is perpendicular to the surface which also endorses the clear peaks in the density profile. On the other hand, at lower α values (α = 0.223 and 0.125), the contact layer ice-like molecules not only form a hexagonal structure of ice but also form smaller and higher membered networks (other than the hexagon), as shown in Fig. 6B and C (top view). This indicates that a defective crystal is formed above the pillar surfaces, and there is a mismatch of lattice between the top of the pillar surface and the nucleating ice crystal. Such defects can be corroborated by the water density profile as well as by the side view of the snapshots, which are

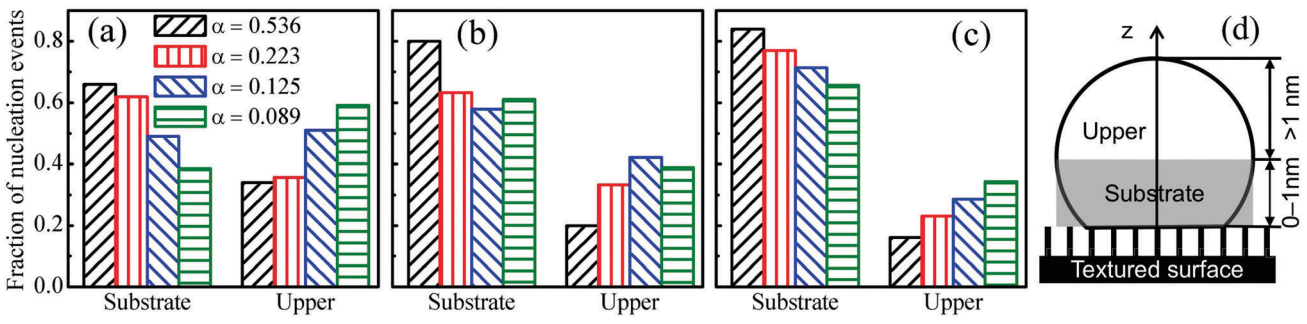

Fig. 5 Distribution of ice nuclei normal to the nanostructured surface as a function of different sizes of clusters: (a) 40–45, (b) 70–75, and (c) 140–150. Distribution is based on the lower boundary along the *z*-axis of an ice cluster and each nucleation event considered when a cluster appears within the spatial region for the first time. (d) Schematic illustration of the substrate (shaded part) and the upper region, which are 0.0–1.0 nm and greater than 1.0 nm above the surface respectively. The color bars black, red, blue and green indicate α = 0.536, 0.223, 0.125, and 0.089 respectively.

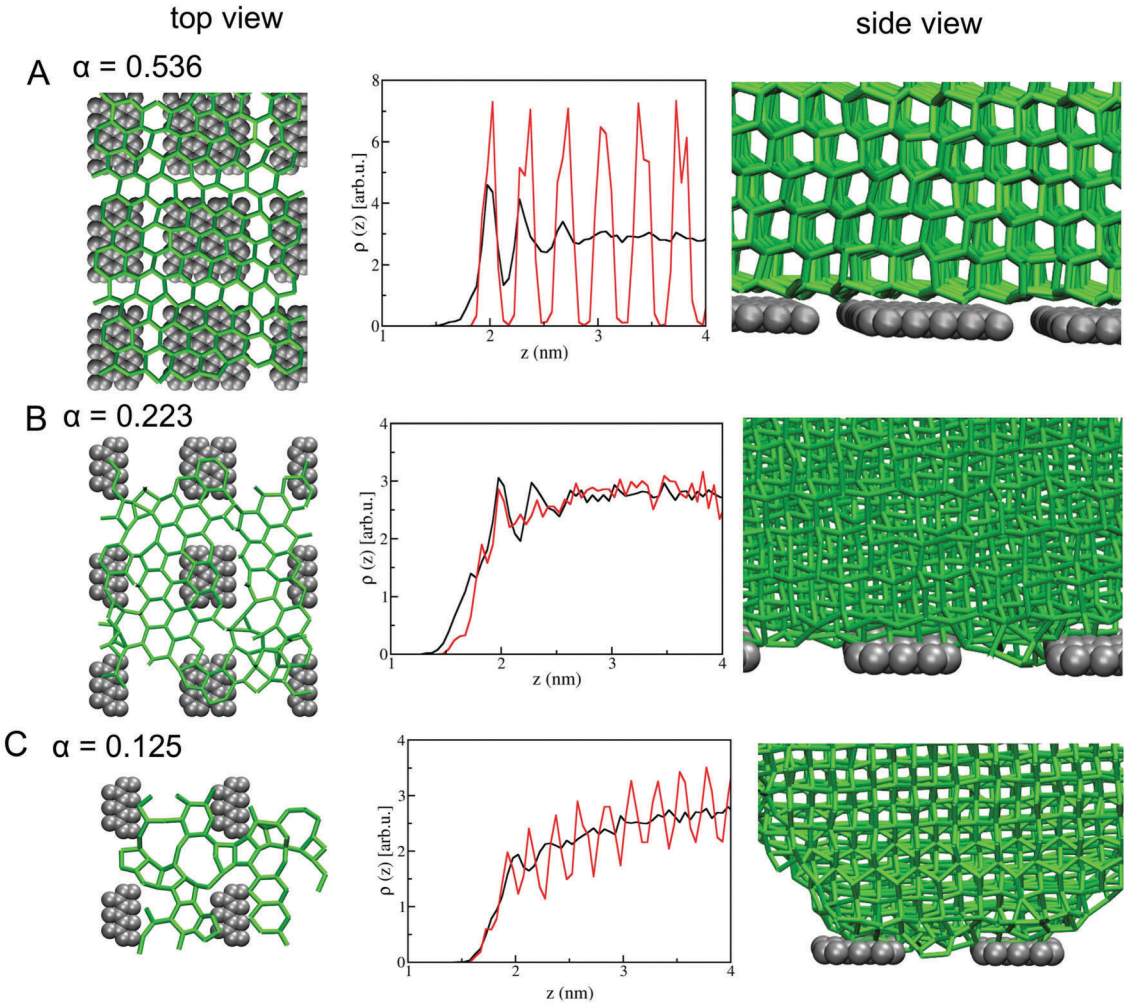

Fig. 6 Representative snapshots of nucleation events and calculated density profiles of water above the surface (bottom of the base and top of the pillar are at z = 0 and 1.7 nm, respectively) for (A) α = 0.536, (B) α = 0.223, and (C) α = 0.125. In the density profile, black and red lines represent the densities of water molecules before and after crystallization. Surface atoms are represented as solid balls (gray color), while the bonding network of water molecules in the ice cluster is depicted by sticks (green lines).

depicted in Fig. 6B and C. Thus, at lower α values the structure of the top of the pillar surface does not act to promote nucleation. We also observed that at lower α values, the nucleation starts either away from the top of the pillar surface or near the vapor–liquid interfacial region and grows downward to the solid–water interface (sec Fig. 4C and D). Therefore, at lower values of α, the contact area between the water and the substrate decreases resulting in the reduction of the nucleation rate. Recent experimental studies on super-hydrophobic surfaces with different roughness factors of nanostructures have reported that the decrease in the contact area enhances the freezing delay time and lowers the nucleation temperature as well as the rate of nucleation.[14,47]

The ice nucleation and crystallization in the bulk water, as well as in water nanodroplets, have been studied extensively by both experiments and simulations.[11,35,36,48,49] It is well known that ice contains several distinct polymorphs.[50] The most common ice crystals are observed as cubic (I_c) and hexagonal (I_h) structures under ambient pressure. Various studies on ice crystallization suggest that cubic ice is favored in the nanometer size water droplet in the temperature range of 160–220 K[51] and has a lower energy barrier to form I_c as compared to the hexagonal ice.[34,52] In this work, we have calculated the ratio of the cubic ice to the hexagonal ice in the cylindrical water droplet, which is shown in Fig. 7. At α = 0.536, the average cubic to hexagonal ratio is around 3.1, whereas at a lower α value (α = 0.089) it is around 2.52, and is comparable to the value of 2.5, reported for ice in a water nanodroplet at 200 K.[11] Our simulation results indicate that the ratio of cubic ice to hexagonal ice of a water droplet appears to be independent of surface fraction of nanostructured surfaces, considering large fluctuation in the values. This is akin to the ratio found for the freezing of water in the bulk and in the nanodroplet.[11]

We also attempt to understand the nucleation behavior of water in the Wenzel state for different α values (akin to that used for the Cassie–Baxter state). At α = 0.223 and 0.125, the computed rate of nucleation does not exhibit a significant difference upon change in the wetting state (*i.e.* from a Cassie–Baxter state to a Wenzel state)

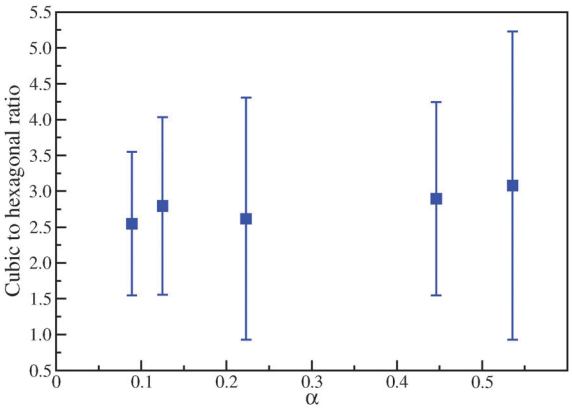

Fig. 7 The ratio of cubic to hexagonal ice in the water cylinder on nanotextured surfaces. The average values are evaluated from 50 independent simulations. The error bars are the standard deviations of 50 simulations.

as shown in Fig. 3. At α = 0.223 and 0.125, the ice-like water molecules within the grooves are unable to form a hexagonal ice structure; thus, do not participate in further promoting the nucleation events as shown in Fig. 8A and B. Further, we have seen that the nucleation events start either in the vicinity of the top of the pillar in the heterogeneous pathway or start near the vapor–liquid interface. On the other hand, at a lower α value, α = 0.089, the calculated nucleation rate increases significantly (see Fig. 3). This is due to the different onset of nucleation behavior from that seen for higher α values. At α = 0.089, Fig. 8C shows that the amount of ice-like water molecules inside the groove increases resulting in six-membered ice-structures. This leads to the decrease of the nucleation energy barrier and thus a higher nucleation rate is observed at α = 0.089. The nucleation event is found to start inside the groove as well as on the top of the pillar. These observations are indeed consistent with a previous study,[37] which reported that the ice nucleation rate gets enhanced remarkably when the groove width matches well with the specific length of the ice crystal. This is also in line with the prediction of rapid crystal nucleation of a hard-sphere model[53] on a surface with nanoscale rough pits with an optimal size.

Now, we turn our attention to the investigation of the effect of the height of nanopillar on the ice nucleation rate for the Cassie–Baxter state. The height of the nanopillar plays a vital role in the wetting behavior of pure fluids and mixtures on rough surfaces.[40,54] Fig. 9 shows the computed rate of nucleation for pillar heights, h = 1.36, 2.72, and 4.08 nm with different α values (α = 0.536, 0.223 and 0.125). We found that the nucleation rate is not very sensitive to the increasing pillar height up to a certain height of the nanopillar (h = 2.72). A further increase in the pillar height is found to increase the nucleation rate. In order to ascertain the reasons behind it,

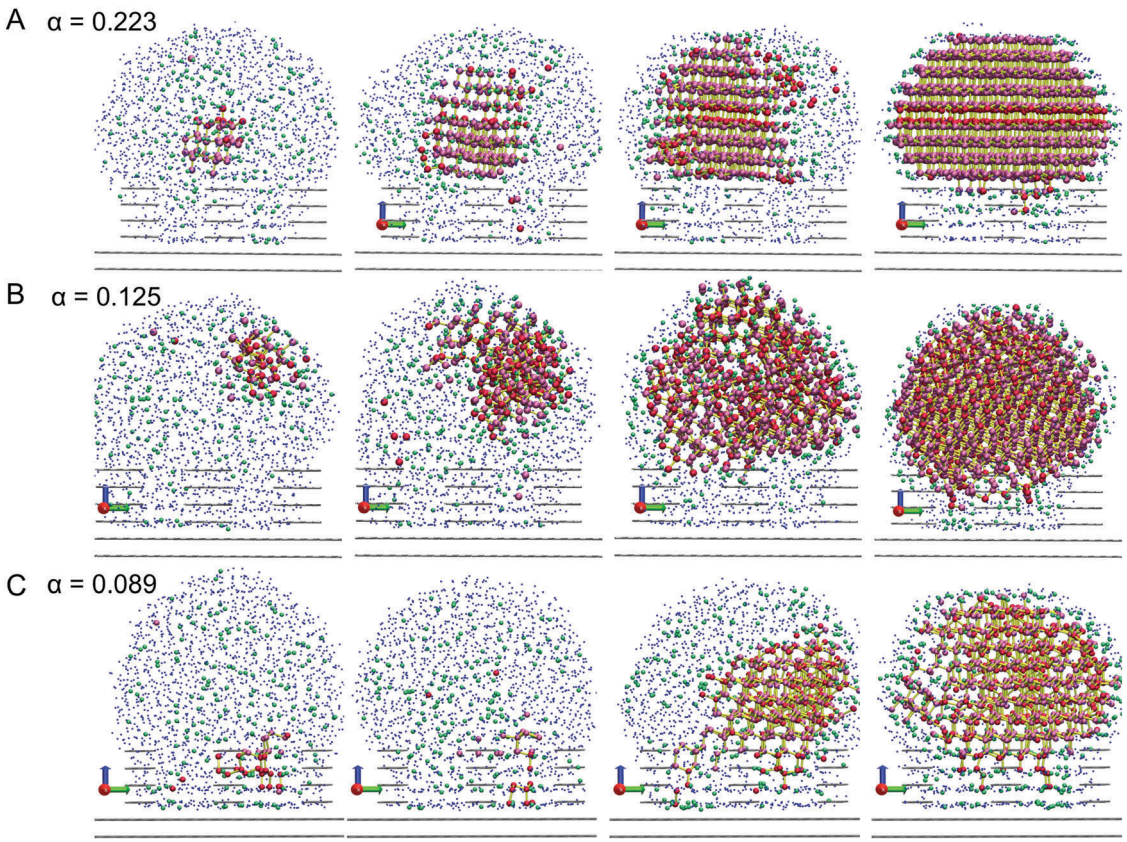

Fig. 8 Snapshots of a supercooled water droplet on nanostructured surfaces, in the Wenzel state, at different stages of crystallization for different surface fractions. (A) α = 0.223, (B) α = 0.125, and (C) α = 0.089. The colors light red, red, green and blue represent water molecules in cubic ice, hexagonal ice, intermediate ice and liquid water, respectively.

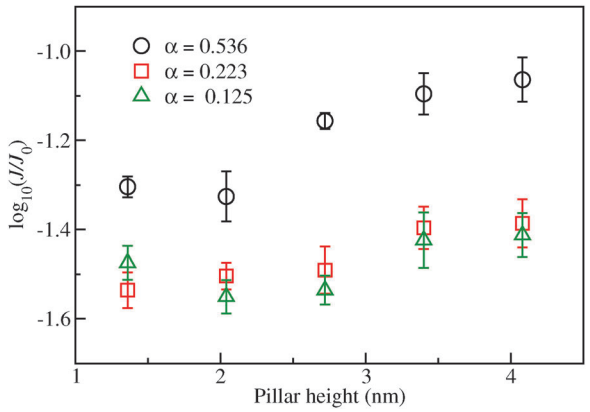

Fig. 9 The ice nucleation rate as a function of pillar height at 203 K, for the Cassie–Baxter state with different surface fractions. The values of the ice nucleation rate are expressed as $\log_{10}(J/J_0)$, where J_0 refers to the nucleation rate of bulk water at the same temperature. The error bars are the standard deviation of the block averages.

we studied the microscopic details of nucleation and growth of ice clusters. Fig. 10 shows the distributions for different sizes of the cluster at different stages of ice nuclei formation along the z-axis above the surface. At $\alpha = 0.536$, initially, the small size clusters are distributed near the surface as well as away from the surface. As the ice nuclei grow, the fraction of nucleation events located near the substrate increases with increasing pillar heights. Such tendency is more noticeable for a higher α value ($\alpha = 0.536$) as compared to a lower α value ($\alpha = 0.125$). Furthermore, to analyse the formation of ice nuclei at different locations, the probability distribution of the ice cluster at different stages of nuclei formation are plotted as a function of distance along the z-direction from the top of the surface (see the ESI,† Fig. S5 and S6). An increase in the pillar height increases the propensity to form large ice clusters near the solid–liquid interface (see Fig. S5(f) and S6(f), ESI†) which is conspicuous by the increased nucleation rate with pillar height. Further, we evaluated the base contact area between the water droplets and the nanostructured surfaces for different heights. As per nucleation theory, the nucleation rate should increase with increasing contact area. The simulation results are found to be in line with the expectation *i.e.*, the contact area increases with increasing pillar height (Fig. S7 and S8, ES†). Recent experimental studies[22] suggest that the significant enhancement of nucleation rate on the nanotextured surface is due to ice nucleation not at the water–substrate interface, but to some extent at the three-phase contact line. However, we did not find any corroboration of enhancement of the nucleation rate due to the tendency of ice nucleation at the water–vapor interface. Our MD study, therefore, indeed supports experimental[22] observations which report the nucleation events at the substrate–water interface as well as at the substrate–water–vapor interface.

To this end, we have performed the work required to remove the ice droplet from nanostructured surfaces using the phantom-wall method[55,56] in order to provide a comprehensive understanding of ice adhesion in different wetting states. We have evaluated the difference in surface free energy ΔF between an actual system where a crystallised droplet sits on a nanostructured surface and a reference system where the crystallised

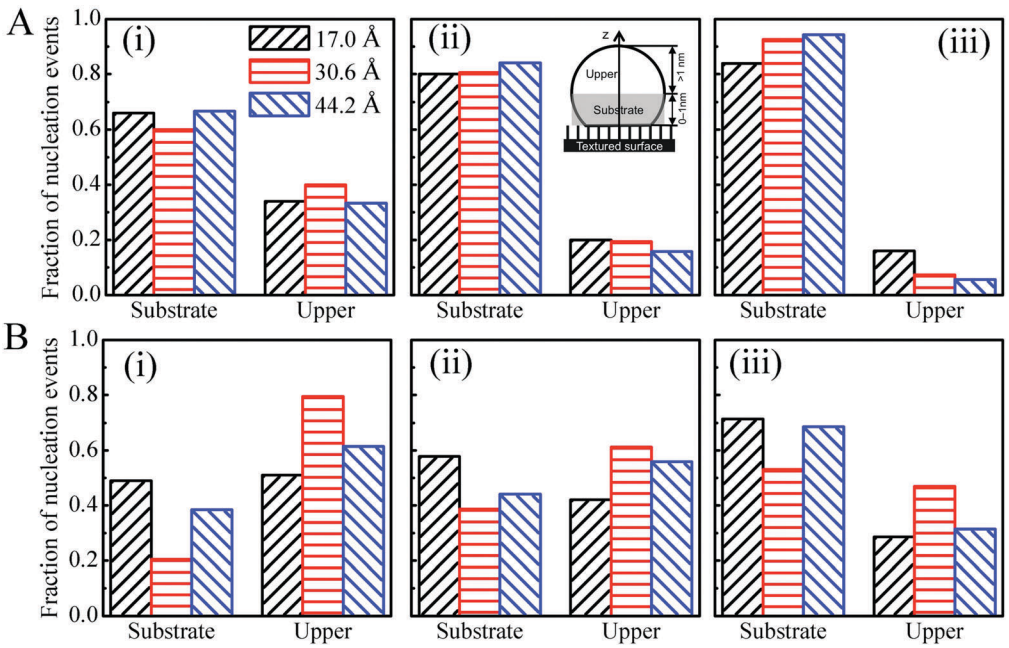

Fig. 10 Distribution of cluster formation at different stages of ice nucleation on the nanostructured surfaces as a function of the cluster size (i) 40–45, (ii) 70–75, and (iii) 140–150 for (A) $\alpha = 0.536$ and (B) $\alpha = 0.125$ for the Cassie–Baxter state. Distribution is based on the lower boundary along the z-axis of an ice cluster and each nucleation event is considered to occur when a cluster appears in the spatial region for the first time. The regions, substrate and upper are for 0.0–1.0 nm and greater than 1.0 nm above the surface, respectively (see inset figure). The color bars black, red, and blue represent the pillar height, h = 1.36, 2.72, and 4.08 nm respectively.

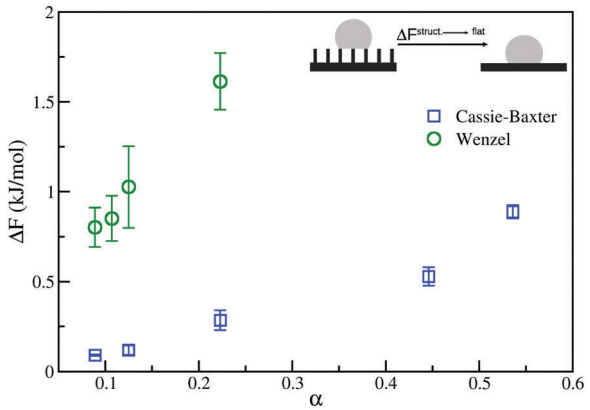

Fig. 11 Variation of the surface free energy difference with respect to α for nanostructured surfaces with different wetting states. The average ΔF values and the corresponding error bars, based on standard deviation, are evaluated from 4 to 6 independent simulations.

droplet contacts with a flat repulsive wall. Here, we have considered a graphite-like flat surface as the reference system, which interacts with water *via* a purely repulsive Weeks–Chandler–Andersen (WCA) potential.[57] A detailed description of the phantom-wall algorithm is presented in the ESI.† Fig. 11 shows the free energy difference ΔF, computed from the phantom-wall method, as a function of α for a supercooled water droplet in the Cassie–Baxter and Wenzel states. Here, our aim is to provide a quantitative information on the work of ice adhesion for different surfaces. A higher ΔF value indicates that a larger amount of work is needed to detach the ice nuclei from the nanostructured surfaces. The results clearly indicate that ΔF increases with α for both the wetting states. It is clear from Fig. 11 that the Wenzel state has higher ice adhesion compared to the Cassie–Baxter state for a given α value. Further, it can be observed that the smooth surface leads to the highest work of ice adhesion. We have found that both the ice adhesion and the rate of ice nucleation are increased with increasing α. On the other hand, the change in ΔF is much higher for the case of Wenzel state. The difference in ΔF values between the two wetting states is approximately 2 times higher at $\alpha = 0.125$ than at $\alpha = 0.089$. The work of adhesion enhances with increasing α, while an opposite behavior is found for the rate of ice nucleation with α. Thus, the nucleation rate does not correlate well with the ice adhesion, which is in line with the earlier work of Singh and Müller-Plathe.[20] In a previous work,[56] it was shown that the work of adhesion is linearly related to the contour length of a liquid droplet in the Wenzel state. However, it is not known if such a behavior also holds for supercooled water droplets. In order to address the above query, we have calculated the total contour length of each contour for the Wenzel system. We have found that ΔF increases with an increase in the contour length as shown in Fig. S9 (ESI†). This is in line with the observation of Leroy and Müller-Plathe.[56] The current work clearly suggests that the solid–liquid work of adhesion in relation to the contour length of droplets on rough surfaces is indeed extensible to ice on the nanostructured surfaces, indicating generalization of such behavior.

4 Conclusions

We have investigated the ice nucleation of a supercooled cylindrical water droplet on nanotextured surfaces at 203 K for the Cassie–Baxter and Wenzel states using molecular dynamics simulations. The simulation results suggest that the ice nucleation rate is enhanced with increasing surface fraction for the Cassie–Baxter state. On the other hand, the nucleation rate decreases for the Wenzel state with increasing surface fraction. In the case of the Cassie–Baxter state, at higher α values ($\alpha > 0.223$), heterogeneous ice nucleation is observed, whereas at lower α values, there are two different pathways of ice nucleation *i.e.* homogeneous and heterogeneous. The highest nucleation rate is found at $\alpha = 0.089$ in the case of the Wenzel state. We have observed that when the length of the ice crystal matches the accessible width of the groove, the nucleation rate is enhanced significantly, which is consistent with the previous finding. In the case of the Cassie–Baxter state, the propensity to form smaller size ice clusters (40–45) is reduced with α within 1.0 nm from the top of the nanostructured surface; whereas the histogram distribution values of the ice cluster increase with an increase in α above 1.0 nm from the surface. We also studied the effect of nanopillar height on ice nucleation and observed that the rate enhances with increasing pillar height. We have evaluated ice adhesion for different nanostructured surfaces. The ice adhesion is significantly higher for the Wenzel state compared to the Cassie–Baxter state. The results presented in this work shed light on the effect of wetting states, surface fraction, and pillar height on the ice nucleation behavior on nanotextured surfaces. We believe that the current work will augment our understanding of the nucleation mechanism at the molecular level for surface design.

Acknowledgements

This work was supported by the Department of Science and Technology (DST), Government of India. The computational resources are provided by the HPC cluster of the Computer Center (CC), Indian Institute of Technology Kanpur. This work was partially supported by Alexander von Humboldt Foundation and SFB-TRR75 of the DFG.

References

1 Y. Diao, T. Harada, A. S. Myerson, T. A. Hatton and B. L. Trout, *Nat. Mater.*, 2011, **10**, 867–871.
2 R. P. Sear, *Int. Mater. Rev.*, 2012, **57**, 328–356.
3 A. Tabazadeh, Y. S. Djikaev and H. Reiss, *Proc. Natl. Acad. Sci. U. S. A.*, 2002, **99**, 15873–15878.
4 B. J. Murray, D. Sullivan, J. D. Atkinson and M. E. Webb, *Chem. Soc. Rev.*, 2012, **41**, 6519–6554.
5 A. Lintunen, T. Hölttä and K. Kulmala, *Sci. Rep.*, 2013, **3**, 2031.
6 T. Li, D. Donadio, L. M. Ghiringhelli and G. Galli, *Nat. Mater.*, 2009, **8**, 726–730.
7 L. Lupi, A. Hudait and V. Molinero, *J. Am. Chem. Soc.*, 2014, **136**, 3156–3164.

8 T. M. Schutzius, S. Jung, T. Maitra, P. Eberle, C. Antonini, C. Stamatopoulos and D. Poulikakos, *Langmuir*, 2015, **31**, 4807–4821.
9 X.-X. Zhang, M. Chen and M. Fu, *Appl. Surf. Sci.*, 2014, **313**, 771–776.
10 S. J. Cox, S. M. Kathmann, B. Slater and A. Michaelides, *J. Chem. Phys.*, 2015, **142**, 184704.
11 J. C. Johnston and V. Molinero, *J. Am. Chem. Soc.*, 2012, **134**, 6650–6659.
12 A. J. Meuler, G. H. McKinley and R. E. Cohen, *ACS Nano*, 2010, **4**, 7048–7052.
13 P. Guo, Y. Zheng, M. Wen, C. Song, Y. Lin and L. Jiang, *Adv. Mater.*, 2012, **24**, 2642–2648.
14 P. Eberle, M. K. Tiwari, T. Maitra and D. Poulikakos, *Nanoscale*, 2014, **6**, 4874–4881.
15 S. Jung, M. Dorrestijn, D. Raps, A. Das, C. M. Megaridis and D. Poulikakos, *Langmuir*, 2011, **27**, 3059–3066.
16 A. B. D. Cassie and S. Baxter, *Trans. Faraday Soc.*, 1944, **40**, 546–551.
17 R. N. Wenzel, *Ind. Eng. Chem.*, 1936, **28**, 988–994.
18 A. Alizadeh, M. Yamada, R. Li, W. Shang, S. Otta, S. Zhong, L. Ge, A. Dhinojwala, K. R. Conway, V. Bahadur, A. J. Vinciquerra, B. Stephens and M. L. Blohm, *Langmuir*, 2012, **28**, 3180–3186.
19 K. Li, S. Xu, W. Shi, M. He, H. Li, S. Li, X. Zhou, J. Wang and Y. Song, *Langmuir*, 2012, **28**, 10749–10754.
20 J. K. Singh and F. Müller-Plathe, *Appl. Phys. Lett.*, 2014, **104**, 021603.
21 T.-S. Wong, S. H. Kang, S. K. Y. Tang, E. J. Smythe, B. D. Hatton, A. Grinthal and J. Aizenberg, *Nature*, 2011, **477**, 443–447.
22 Q. T. Fu, E. J. Liu, P. Wilson and Z. Chen, *Phys. Chem. Chem. Phys.*, 2015, **17**, 21492–21500.
23 M. Nosonovsky and V. Hejazi, *ACS Nano*, 2012, **6**, 8488–8491.
24 P. Hao, C. Lv and X. Zhang, *Appl. Phys. Lett.*, 2014, **104**, 161609.
25 S. Jung, M. K. Tiwari, N. V. Doan and D. Poulikakos, *Nat. Commun.*, 2012, **3**, 615.
26 S. Auer and D. Frenkel, *Phys. Rev. Lett.*, 2003, **91**, 015703.
27 D. Moroni, P. R. ten Wolde and P. G. Bolhuis, *Phys. Rev. Lett.*, 2005, **94**, 235703.
28 M. Matsumoto, S. Saito and I. Ohmine, *Nature*, 2002, **416**, 409–413.
29 E. B. Moore and V. Molinero, *J. Chem. Phys.*, 2010, **132**, 244504.
30 P. Pirzadeh and P. G. Kusalik, *J. Am. Chem. Soc.*, 2011, **133**, 704–707.
31 E. B. Moore and V. Molinero, *Nature*, 2011, **479**, 506–508.
32 T. Li, D. Donadio, G. Russo and G. Galli, *Phys. Chem. Chem. Phys.*, 2011, **13**, 19807–19813.
33 A. Reinhardt and J. P. K. Doye, *J. Chem. Phys.*, 2012, **136**, 054501.
34 R. Radhakrishnan and B. L. Trout, *J. Am. Chem. Soc.*, 2003, **125**, 7743–7747.
35 T. Li, D. Donadio and G. Galli, *Nat. Commun.*, 2013, **4**, 1887.
36 J. R. Espinosa, E. Sanz, C. Valeriani and C. Vega, *J. Chem. Phys.*, 2014, **141**, 18C529.
37 X.-X. Zhang, M. Chen and M. Fu, *J. Chem. Phys.*, 2014, **141**, 124709.
38 R. Cabriolu and T. Li, *Phys. Rev. E: Stat., Nonlinear, Soft Matter Phys.*, 2015, **91**, 052402.
39 M. Fitzner, G. C. Sosso, S. J. Cox and A. Michaelides, *J. Am. Chem. Soc.*, 2015, **137**, 13658–13669.
40 T. Koishi, K. Yasuoka, S. Fujikawa, T. Ebisuzaki and X. C. Zeng, *Proc. Natl. Acad. Sci. U. S. A.*, 2009, **106**, 8435–8440.
41 V. Molinero and E. B. Moore, *J. Phys. Chem. B*, 2009, **113**, 4008–4016.
42 S. Plimpton, *J. Comput. Phys.*, 1995, **117**, 1–19.
43 E. B. Moore, E. de la Llave, K. Welke, D. A. Scherlis and V. Molinero, *Phys. Chem. Chem. Phys.*, 2010, **12**, 4124–4134.
44 J. Wedekind, R. Strey and D. Reguera, *J. Chem. Phys.*, 2007, **126**, 134103.
45 L. C. Jacobson, W. Hujo and V. Molinero, *J. Phys. Chem. B*, 2009, **113**, 10298–10307.
46 L. Vrbka and P. Jungwirth, *J. Phys. Chem. B*, 2006, **110**, 18126–18129.
47 L. Boinovich, A. M. Emelyanenko, V. V. Korolev and A. S. Pashinin, *Langmuir*, 2014, **30**, 1659–1668.
48 A. Manka, H. Pathak, S. Tanimura, J. Wolk, R. Strey and B. E. Wyslouzil, *Phys. Chem. Chem. Phys.*, 2012, **14**, 4505–4516.
49 H. Laksmono, T. A. McQueen, J. A. Sellberg, N. D. Loh, C. Huang, D. Schlesinger, R. G. Sierra, C. Y. Hampton, D. Nordlund, M. Beye, A. V. Martin, A. Barty, M. M. Seibert, M. Messerschmidt, G. J. Williams, S. Boutet, K. Amann-Winkel, T. Loerting, L. G. M. Pettersson, M. J. Bogan and A. Nilsson, *J. Phys. Chem. Lett.*, 2015, **6**, 2826–2832.
50 V. Buch, R. Martoák and M. Parrinello, *J. Chem. Phys.*, 2006, **124**, 204705.
51 G. P. Johari, *J. Chem. Phys.*, 2005, **122**, 194504.
52 D. Quigley and P. M. Rodger, *J. Chem. Phys.*, 2008, **128**, 154518.
53 J. A. van Meel, R. P. Sear and D. Frenkel, *Phys. Rev. Lett.*, 2010, **105**, 205501.
54 A. K. Metya, S. Khan and J. K. Singh, *J. Phys. Chem. C*, 2014, **118**, 4113–4121.
55 F. Leroy, D. J. V. A. dos Santos and F. Müller-Plathe, *Macromol. Rapid Commun.*, 2009, **30**, 864–870.
56 F. Leroy and F. Müller-Plathe, *Langmuir*, 2011, **27**, 637–645.
57 J. D. Weeks, D. Chandler and H. C. Andersen, *J. Chem. Phys.*, 1971, **54**, 5237–5247.

